

# Properties of Vertical Ground Motions

by Igor A. Beresnev, Amber M. Nightengale, and Walter J. Silva

**Abstract** A typical engineering approach to developing site-specific design vertical ground motions starts with rock-outcrop horizontal motions, converts them into the vertical component using an empirical vertical-to-horizontal (V/H) ratio for response spectra, and propagates the resulting motion through the soil column as a vertically incident  $P$  wave. In the absence of data on strain-dependent soil properties in compressional deformation, strain-compatible shear-wave properties from the horizontal-component analyses are utilized. This approach makes two assumptions: (1) that the vertical motions are primarily composed of compressional waves and (2) that strain-dependent material properties in shear deformation can be extrapolated to compressional deformation. Our study deals with the empirical validation of both assumptions. First, we investigated the ratio of  $SV$ - to  $P$ -wave spectra of the vertical component of ground motions from significant recent events in California to find which wave type predominantly contributed to vertical motions, in the frequency range of 0.5–25 Hz. The results indicate that shear waves dominate the vertical motions at frequencies up to approximately 10 Hz, above which the contribution of compressional deformation is about as strong or greater. This result holds for both soil and rock sites. Second, using the data from the KiK-net borehole arrays in Japan, we estimated the nonlinearity in compressional deformation by studying  $P$ -wave amplification at variable amplitude levels. Frequency shifts and in some instances reduced amplification, compatible with the hysteretic softening type of nonlinearity known for shear waves, is found as the amplitude of compressional strain increases. A tentative curve of constrained-modulus reduction is also similar to the existing shear-modulus reduction curves.

The results of this study suggest that, for most practical applications, vertical motions can be modeled as nonvertically propagating  $SV$  waves. This could be implemented through conventional one-dimensional horizontal-component modeling using SHAKE and the application of empirical depth-dependent V/H correction factors to account for the inclined propagation path. At high frequencies, vertical motions may have to be modeled as near-vertically propagating  $P$  waves, with strain-dependent properties specifically developed for compressional deformation; however, these frequencies may be of lesser importance for design applications.

## Introduction

Proper characterization of site-specific design vertical ground motions is required in a variety of engineering applications. The importance of this task has been emphasized by a recent observation that vertical motions can exceed horizontal motions at short periods and near-source distances (Electric Power Research Institute [EPRI], 1993; Bozorgnia *et al.*, 1995; Silva, 1999). However, the specification of vertical motions, as compared to horizontal motions, is not nearly as well understood. A typical engineering approach (e.g., EPRI, 1993; Silva, 1999, and references therein) starts with horizontal rock-outcrop motions and applies an empirical vertical-to-horizontal spectral (V/H) ratio, established

from surface records, to convert them into the vertical component in the frequency domain. The resulting vertical motion, transformed back to the time domain, is then propagated vertically as a compressional ( $P$ ) wave time history through a specified soil column, generally using the program SHAKE (Schnabel *et al.*, 1972; Idriss and Sun, 1992). For the lack of empirical constraints, the possible  $P$ -wave nonlinearity is accounted for by extrapolating the strain-dependent velocity and damping, developed for shear waves, into compressional deformation using the relationships between  $P$ - and  $S$ -wave velocities and quality factors known from linear elasticity.

As seen from above, the existing approach postulates, first, that the vertical motions are primarily comprised of  $P$ , not  $SV$ , waves. This would be true for the vertical propagation; however, even a small nonzero incidence angle would make contribution from  $SV$  waves rather strong, keeping in mind the large amplitudes of shear motion. The second assumption is that the nonlinearity in compressional deformation can be modeled as a scaled version of shear-wave nonlinearity, which cannot generally be true. The nonlinearity in compressional deformation may be described by a different type of constitutive law, which may not resemble the nonlinear rheology in shear. To develop a more rigorous model of vertical motions, one has to validate both assumptions.

These two issues are addressed in our work through the analyses of available strong-motion data. First, we consider the question of relative contribution of  $P$  and  $SV$  waves to the vertical component of ground motions. Second, using the recent borehole data from Japan, we study the possible manifestations of constitutive-law nonlinearity in  $P$  waves. The implications of the study are discussed in the context of the improvement in the existing engineering models of vertical motions.

### Contribution of $P$ and $SV$ Waves to Vertical Motions

The relative contribution of compressional and shear waves to vertical motions, as a function of frequency, can be determined by the analysis of the spectra of surface motions in respective time windows. Using the strong-motion database of Pacific Engineering and Analysis, we studied the surface records of the five most significant recent earthquakes in California, at both rock and soil sites. The sites were classified according to the Geomatrix scheme: those assigned the Geomatrix categories A and B (“generic rock and soft rock”) were grouped as rock sites, and those in categories C and D (“generic soil”) were grouped as soil. A total of 279 soil and 109 processed rock records from the 1983  $M$  6.4 Coalinga, 1987  $M$  6.1 Whittier Narrows, 1989  $M$  7.0 Loma Prieta, 1992  $M$  7.3 Landers, and 1994  $M$  6.7 Northridge earthquakes were utilized.

The original traces had different sampling rates. To utilize all the data available, we low-pass filtered and decimated the traces to a common (largest) sampling interval of 0.02 sec. Because it corresponds to the Nyquist frequency of 25 Hz, the cutoff frequency of the low-pass filter was set at 12.5 Hz to avoid aliasing effects. To extend the high-frequency limit of the analysis, we also selected a smaller subset of the data with the higher sampling rates, allowing decimation to 0.01 sec. This subset included 158 soil and 80 rock records. By choosing the frequency of the antialiasing filter using the same rule, the frequency range of the analysis was extended to 25 Hz.

On the vertical-component records, we identified the  $P$ - and  $SV$ -wave windows. Because our goal was to study the ratio of these waves’ spectral densities, we needed to make

sure that the spectra were calculated in a consistent manner. The length of the  $P$ -wave window, ending at the  $S$ -wave arrival, was variable depending on the distance from the source. To ensure comparability of the spectra, the  $P$ -wave window length was measured first and then the identical length of the  $S$ -wave window was taken. The windows were then cosine tapered, and their Fourier amplitude spectra were calculated. The spectra were smoothed using a running three-point weighted (0.25-0.5-0.25) average. For the 0.02- and 0.01-sec decimated data, the spectra were sampled at 0.0122 and 0.0244 Hz, respectively. We used visual judgment to determine the number of runs needed to achieve optimum smoothing. We used 80 runs in  $SV$ - and  $P$ -wave spectra calculations. Finally, the ratios of spectra between the  $SV$  and  $P$  windows ( $SV/P$ ) were calculated in the frequency band of 0.5–12.5 Hz (the full set of traces) and 0.5–25 Hz (the higher-sampling-rate subset of stations).

The above  $SV/P$ -ratio calculation procedure assumes that the  $P$ -wave window, identified from the traces, is predominantly composed of  $P$  waves. The validity of this assumption seems obvious, although it does not preclude the presence of  $SV$ -wave energy from  $P$ -wave conversion at the base of near-surface layer. The significance of this contribution can be estimated as follows.

Let us assume a  $P$ -wave incident from below upon an interface separating two media characterized by  $\alpha_2$ ,  $\beta_2$ , and  $\rho_2$  (the lower medium) and  $\alpha_1$ ,  $\beta_1$ , and  $\rho_1$  (the upper medium), where  $\alpha$ ,  $\beta$ , and  $\rho$  are the compressional- and shear-wave velocities and density, respectively. The incidence angle is  $i_2$ . The wave produces  $P$ - and  $SV$ -transmitted waves at the refraction angles  $i_1$  and  $j_1$ , with the displacement transmission coefficients  $P'P'$  and  $P'S'$ , respectively, whose values can be determined for a given  $i_2$  (e.g., Aki and Richards [1980], equations 5.39, original notation is kept for media parameters and transmission coefficients). The angles  $i_1$  and  $j_1$  can be found from Snell’s law.

Projecting the displacement vector in the transmitted waves onto the vertical axis, one obtains the ratio of their vertical components,

$$\frac{SV_z}{P_z} = \frac{P'S' \sin j_1}{P'P' \cos i_1}. \quad (1)$$

Let us consider an extreme case of large impedance contrast, which would provide the highest efficiency of conversion, for example,  $\alpha_1 = 600$  m/sec,  $\beta_1 = \alpha_1/\sqrt{3}$ ,  $\rho_1 = 1500$  kg/m<sup>3</sup>, and  $\alpha_2 = 2000$  m/sec,  $\beta_2 = \alpha_2/\sqrt{3}$ ,  $\rho_2 = 2000$  kg/m<sup>3</sup>. In this example, the shear-wave velocities were converted from the compressional-wave velocities, and the densities were obtained from the compressional-wave velocities using the empirical Gardner’s rule:  $\rho = a\alpha^{1/4}$ , where  $\alpha$  is in m/sec and  $a = 310$  (Sheriff and Geldart [1995], equation 5.15). It is clear that, due to refraction, the transmitted waves will propagate near-vertically, and the vertical component of the  $SV$  wave will be rather small. An accurate calculation, taking

into account the efficiency of conversion, can be done using equation (1).

The practically observed angles of incidence are expected to be low due to the upper-crustal impedance gradients. For example, for incidence angles  $i_2 = 30^\circ, 20^\circ,$  and  $10^\circ,$  the  $SV_z/P_z$  ratios (1) are 0.039, 0.017, and 0.0043, respectively. The contribution of the converted shear wave to the vertical component is thus not expected to exceed a few percent even for high impedance contrast and relatively large incidence angles, which shows the applicability of our analysis. We also neglect the  $SV$  to  $P$  conversion in the shear-wave window in our analyses.

Figure 1 presents the average spectral ratios between the  $SV$ - and  $P$ -wave windows of the vertical component for (a) soil and (b) rock sites, with 95% confidence interval of the mean and standard deviation. The curves have been obtained from the entire database of soil and rock records decimated to 0.02 sec. The ratios show that the  $SV$  wave dominates the vertical motions on average at lower frequencies at both soil and rock sites. Its contribution is progressively

reduced toward higher frequencies, and at frequencies of about 10 Hz, the average  $P$ -wave contribution is about the same. Figure 1c compares the mean ratios at soil and rock sites using a statistical  $t$ -test of the difference between two means. The bands around the curves are arranged in such a way that, where they do not overlap, the difference between the means is at 95% confidence level. The rock ratio (solid lines) slightly exceeds the soil ratio (dotted lines) between approximately 0.7 and 3 Hz, by a maximum amount of about 0.17 log units (a factor of 1.5); at other frequencies, there is no significant difference.

Figure 2 presents similar  $SV/P$  spectral ratios computed for the subset of the database with the higher sampling rate, with the frequency range extended to 25 Hz. There is no significant difference in the spectral-ratio behavior between Figures 1 and 2 in their common frequency band of 0.5–12.5 Hz; the decreasing contribution of  $SV$  waves to the vertical component is confirmed in Figure 2 to the frequency of 25 Hz.

We also grouped the ratios into distance (<15 km and

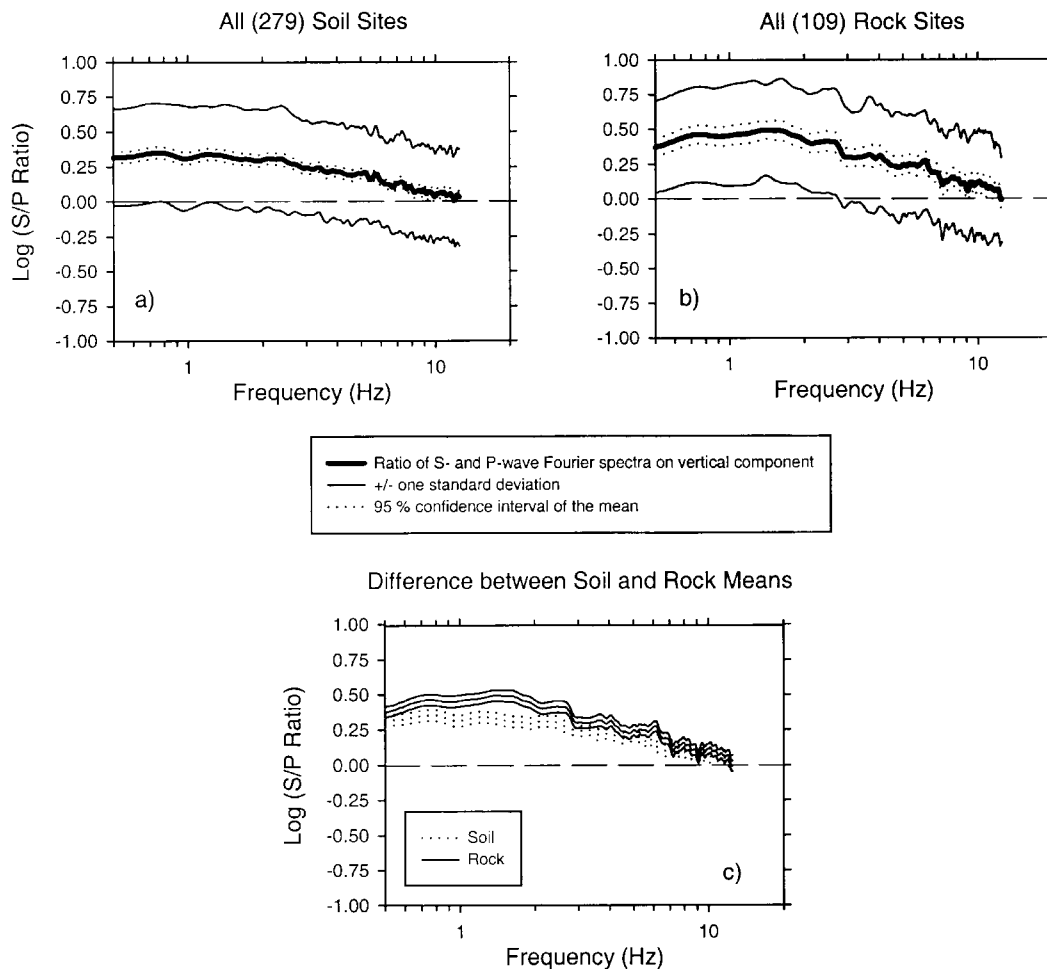


Figure 1. Average ratios of Fourier spectra between  $SV$ - and  $P$ -wave windows on vertical component of ground motions: (a) California soil sites, (b) California rock sites, (c) statistical test of difference between soil and rock means. Curves for the entire database are shown.

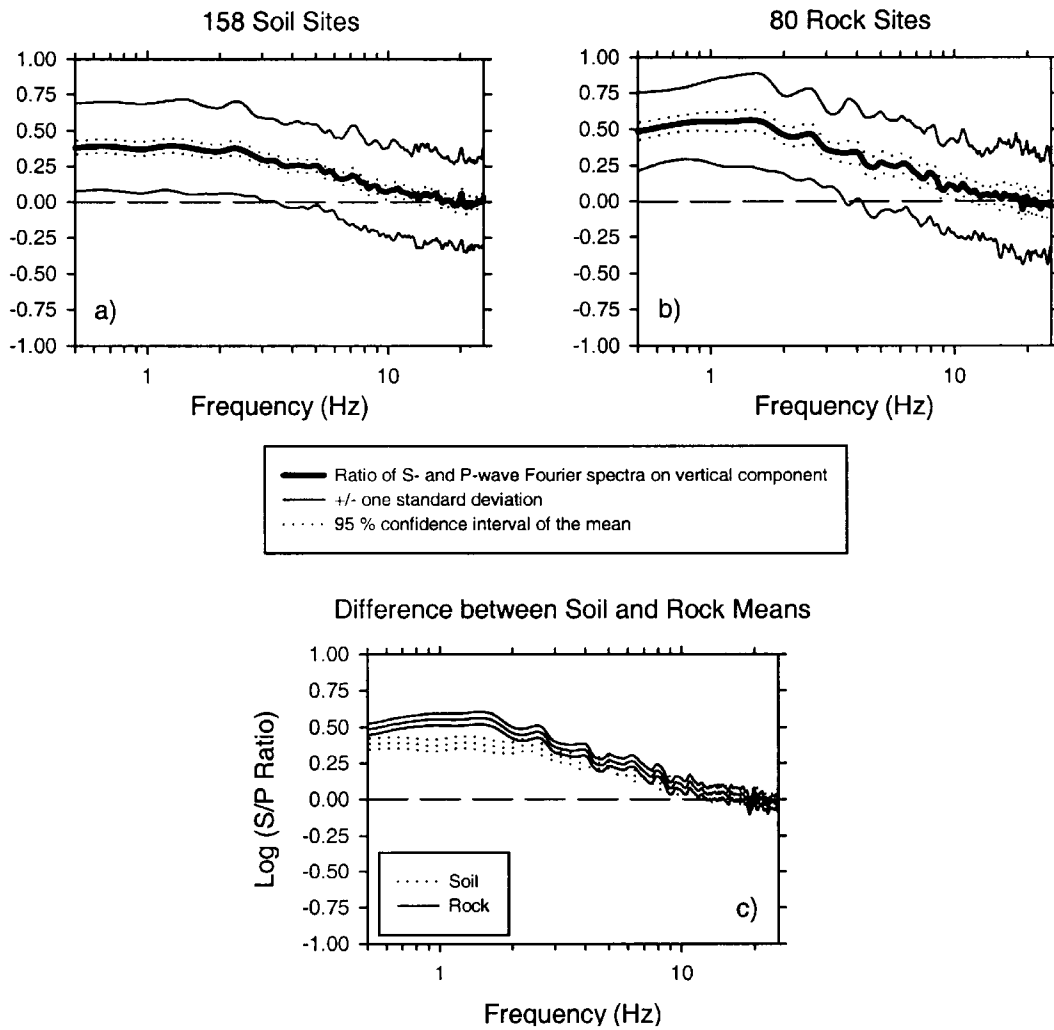


Figure 2. Same as Figure 1 except the curves are shown for the subset of data with the higher sampling rate.

>15 km) and peak-acceleration (<0.1 g and >0.4 g) bins, separately for rock and soil sites, to try to discriminate between the distance and nonlinearity effects, respectively. We have not found any significant differences between the distance or acceleration groups, on rock or on soil. The only difference seen was that between rock and soil similar to that in Figure 1c, in each of the distance or acceleration bins. We concluded that the site category (rock versus soil) was the only significant factor affecting the ratios among those considered. A plausible explanation of lower ratios on soil could be the higher attenuation in *S* waves, which reduces their contribution relative to *P* waves. Another explanation could be in the effect of near-surface refraction, which is greater at soil sites due to their higher velocity gradient, reducing the contribution of *SV* motion (see also inset in Fig. 3).

Based on Figures 1a,b and 2a,b, one can separate the frequency range, in terms of the wave type controlling the vertical motions, into two intervals: below ~10 Hz, where

*SV* waves dominate, and above ~10 Hz, where *P* waves are at least equally strong or may be the dominant motions. This corresponds to a crossover period of about 0.1 sec, at which the nature of vertical motions changes.

Note that, even if the *P* waves dominate the high frequencies, this may not be seen as a clear decrease in the *SV/P* ratio below unity. One should keep in mind that, unlike the *P*-wave window that is almost entirely composed of *P* waves, the *SV*-wave window is a superposition of *SV* waves over a tail of *P* waves. If the distance from the source is sufficiently short, there will be significant *P*-wave energy extending into the *SV*-wave window. At the frequencies where *P* waves dominate, therefore, one will essentially divide the *P*-wave spectrum by the *P*-wave spectrum, obtaining the values close to 1. The lower values can only be expected at longer distances, where only an insignificant portion of *P*-wave energy overlaps with *SV* waves. This shows that one can merely infer from the value of *SV/P* ratio close to unity that the *P* wave is at least as strong as the *SV*

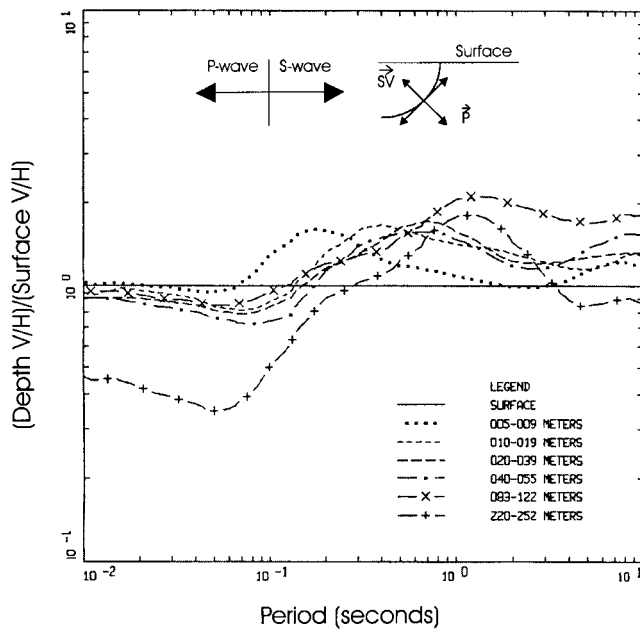


Figure 3. Average V/H response-spectral ratios (5% damping) for six depth ranges, combined from observations at 10 borehole accelerograph arrays. The ratios were normalized by the surface ratio, which plots as the solid line at unity (after Darragh *et al.*, 1999). The inset explains how the contribution of particle motions in SV and P waves changes as the propagation path bends toward the surface. The vertical line marks the transitional frequency at which the wave type primarily contributing to the vertical motions changes.

wave, whereas in reality it may be the dominant motion. The fact that P waves may dominate the frequencies above  $\sim 10$  Hz is supported by the data in Figure 3 (see following discussion).

Darragh *et al.* (1999) studied the depth variation in the response-spectral ratio between the vertical and horizontal (V/H) components of ground motions using the data from 10 vertical arrays in California, Japan, and Taiwan. The data were grouped into six depth bins, and the average ratio was calculated for each of them. Figure 3 presents the average ratios, normalized by that at the surface. The ratios outline two distinct frequency bands where the depth behavior is different. At short periods, the ratios at depth are systematically smaller than those at the surface, whereas at long periods they are larger. The crossover period is between 0.1 and 0.2 sec, coinciding with the above frequency separating the SV- and P-wave contributions. The frequency-dependent depth behavior, found by Darragh *et al.* (1999), finds explanation in the corresponding change in the type of the wave controlling the vertical component. As the inset in Figure 3 schematically demonstrates, the P-wave contribution increases and SV-wave contribution decreases as the wave path bends toward the surface. At frequencies where SV waves dominate (longer periods), one will then find the vertical

component increasing with depth, while at those where P waves dominate (short periods), the pattern will be the opposite. These patterns are seen to the right and to the left of the period of about 0.1 sec in Figure 3, respectively; this transitional period is marked by a vertical line on top of Figure 3. Note that the horizontal component, dominated by SH waves, will remain unaffected. Our data, showing the decreasing effect of SV waves on vertical motions as frequency increases, are thus consistent with the observed depth dependence of V/H ratios.

## Nonlinearity in Compressional Deformation

### Data Used

We analyzed nonlinearity in compressional deformation by studying the near-surface amplification of P waves, as a function of amplitude, using the data from the KiK-net digital borehole accelerograph arrays in Japan (<http://www.kik.bosai.go.jp>). From the KiK-net online database, we selected the boreholes where the recordings of both “weak” and “strong” motions were available (selection current as of May 2001). The weak events were those whose whole-trace peak acceleration was below  $0.1g$  on all components, whereas the strong events were those whose peak acceleration in the P-wave window exceeded  $0.1g$  on at least one vertical component. Four boreholes were identified using these criteria (OKYH09, SMNH01, SMNH02, and TTRH02). Each borehole penetrated a soil layer and ended in rock, with the exception of SMNH02, which was entirely penetrated through rock (granite). Figure 4 shows the lithology of these boreholes arranged in alphabetical order. All boreholes had two instruments: one at the surface and one at the depth of 103 m (OKYH09, TTRH02) or 104 m (SMNH01, SMNH02). All bottom instruments were in rock. Table 1 lists the parameters of all events recorded by the boreholes; the events are arranged in the order of increasing surface peak ground acceleration (PGA) (fourth column). For convenience, the events that did not fall under the weak category are grouped as strong in Table 1, although some of them did not develop peak acceleration in the P-wave window exceeding  $0.1g$ . These intermediate events will be used for control purposes, as explained below. For the same purpose, an additional borehole (NARH01) was included.

The locations of events and boreholes are shown in Figure 5. Most of them are clustered in a limited area in the center of the expanded map. The stars, indicating earthquake epicenters, overlap, showing that the events came from a common source area. All four boreholes recorded the Tottoriken-seibu earthquake, the strongest  $M 7.1$  event, which occurred on 6 October 2000, creating a surface PGA approaching  $1g$ .

### Method and Results

The idea of the method of nonlinearity analysis is to compare the near-surface amplification, calculated from the

KiK-Net Borehole Lithologies

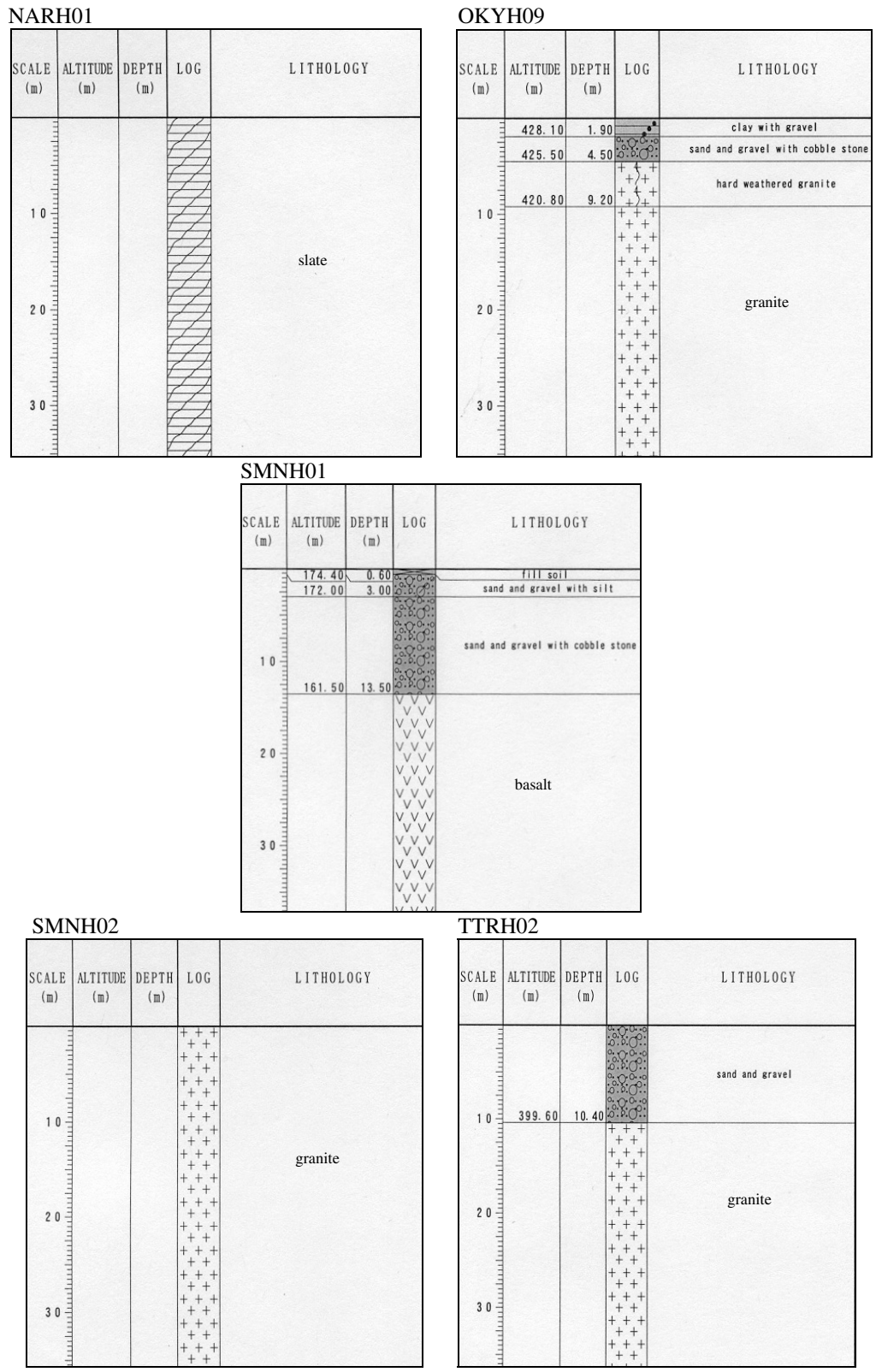


Figure 4. Lithology of KiK-net boreholes used in *P*-wave nonlinearity analyses. Source: KiK-net WWW site (<http://www.kik.bosai.go.jp>).

Table 1  
Selected KiK-Net Events

Event Date and Time (year mddd hr:min)	Magnitude*	Epicentral Distance (km)	Maximum Surface PGA (g)
NARH01 Weak Events			
2000 0602 15:06	4.3	24	.012
2000 0428 11:42	4.5	8	.022
1998 1111 00:27	3.7	23	.029
NARH01/Strong Event			
1999 0821 05:33	5.5	15	.161
OKYH09 Weak Events			
2000 1008 06:21	3.7	26	.003
2000 1007 08:24	3.7	26	.010
2000 1030 15:58	3.7	26	.011
2000 1006 16:25	3.6	17	.012
2000 1006 22:57	4.4	26	.015
2000 1105 03:00	4.0	2.6	.021
2000 1006 16:54	4.0	26	.023
2000 1007 04:59	4.9	29	.032
2000 1017 22:17	4.6	26	.059
OKYH09 Strong Event			
2000 1006 13:30	7.1	29	.289
SMNH01 Weak Events			
2000 1104 04:29	3.5	12	.004
2000 1220 10:04	3.7	12	.006
2001 0122 13:20	3.8	12	.007
2000 1129 21:35	2.9	13	.008
2000 1104 07:15	3.9	12	.013
2001 0116 18:06	3.8	16	.013
2000 1030 15:58	3.7	16	.015
2000 1113 18:32	3.9	12	.015
2000 1219 06:18	4.3	12	.018
2000 1018 08:05	3.9	12	.027
2000 1012 17:07	3.9	3	.029
2000 1104 10:48	3.8	12	.038
2000 1103 16:33	4.7	27	.039
2000 1013 10:44	3.6	13	.040
2000 1014 03:36	3.7	3	.042
2000 1207 23:09	4.5	12	.050
2000 1017 22:17	4.6	16	.051
2000 1006 19:57	4.0	3	.060
2000 1018 14:22	3.8	3	.064
2000 1018 00:00	3.4	3	.068
2000 0717 08:00	4.6	17	.072
2000 1007 06:22	4.2	3	.087
2000 1018 23:39	4.0	11	.090
2000 1010 02:26	3.5	3	.092
2000 1007 07:49	4.3	13	.093
2000 1006 23:13	4.4	3	.096
SMNH01 Strong Events			
2000 1017 22:10	3.7	3	.108
2000 1007 18:32	4.2	3	.159
2000 1007 04:59	4.9	13	.259
2000 1006 13:30	7.1	13	.735
SMNH02 Weak Events			
2000 1007 06:38	4.4	28	.008
2000 1007 07:49	4.3	30	.016
2000 1007 12:03	4.5	28	.018
2000 1006 21:29	4.1	21	.024
2000 1006 19:57	4.0	21	.025
2000 1006 16:38	3.5	30	.027
2000 1007 04:59	4.9	30	.039

Table 1 (continued)

2000 1006 23:13	4.4	21	.046
2000 1010 21:58	4.6	28	.050
SMNH02 Strong Event			
2000 1006 13:30	7.1	30	.575
TTRH02 Weak Events			
2000 1019 08:03	3.8	21	.010
2000 1103 16:53	3.7	21	.010
2000 1129 21:35	2.9	8	.011
2000 1104 10:48	3.8	21	.012
2000 1220 10:04	3.7	21	.015
2001 0122 13:20	3.8	21	.015
2000 1104 07:15	3.9	21	.017
2000 1018 23:39	4.0	9	.022
2000 1113 18:32	3.9	21	.023
2000 1030 15:58	3.7	3	.042
2000 1219 06:18	4.3	21	.042
2000 1207 23:09	4.5	21	.064
2000 1013 10:44	3.6	8	.082
TTRH02 Strong Events			
2001 0116 18:06	3.8	3	.103
2000 1105 03:00	4.0	3	.128
2000 1009 01:14	3.5	3	.135
2000 1017 22:17	4.6	3	.163
2000 1006 13:30	7.1	8	.946

\*Definition of magnitude not found on KiK-net WWW site. Apparently, this is the JMA (Japan Meteorological Agency) magnitude.

records of surface and downhole instruments, between the weak and strong motions. The amplification function is controlled by the wave velocity and damping in soil, which in nonlinear soil become amplitude dependent; the difference in the location of resonance peaks and the value of amplification between the weak and strong motions will then indicate nonlinearity (e.g., EPRI, 1993; Beresnev and Wen, 1996a).

The method of amplification-function calculation is similar to that used by Beresnev and Wen (1995). On baseline-corrected vertical-component records, we identified the *P*-wave window, cosine tapered it, calculated the smoothed Fourier spectrum, and divided the surface spectrum by the downhole spectrum. Smoothing of the spectra was performed similarly to the *SV/P* calculations above. For each borehole, we calculated the average weak-motion amplification for all weak events listed in Table 1; these average functions are plotted in Figure 6 as thin lines, with 95% confidence intervals of the mean (dotted lines). The boreholes are arranged in alphabetical order. Figure 6 also presents the strong-motion amplifications, separately for each of the events listed as strong in Table 1 (thick lines). The strong-event origin time and maximum acceleration in *P*-wave window are listed in the upper left and right corners of the plots, respectively. For each of the four boreholes, there is only one event whose *P*-wave acceleration exceeded 0.1g; this is the *M* 7.1 Tottoriken-seibu earthquake mentioned previously (*P*-wave accelerations of ~115, 255, 120, and 340 cm/sec<sup>2</sup> at OKYH09, SMNH01, SMNH02, and TTRH02, respectively). Figure 7 shows the three compo-

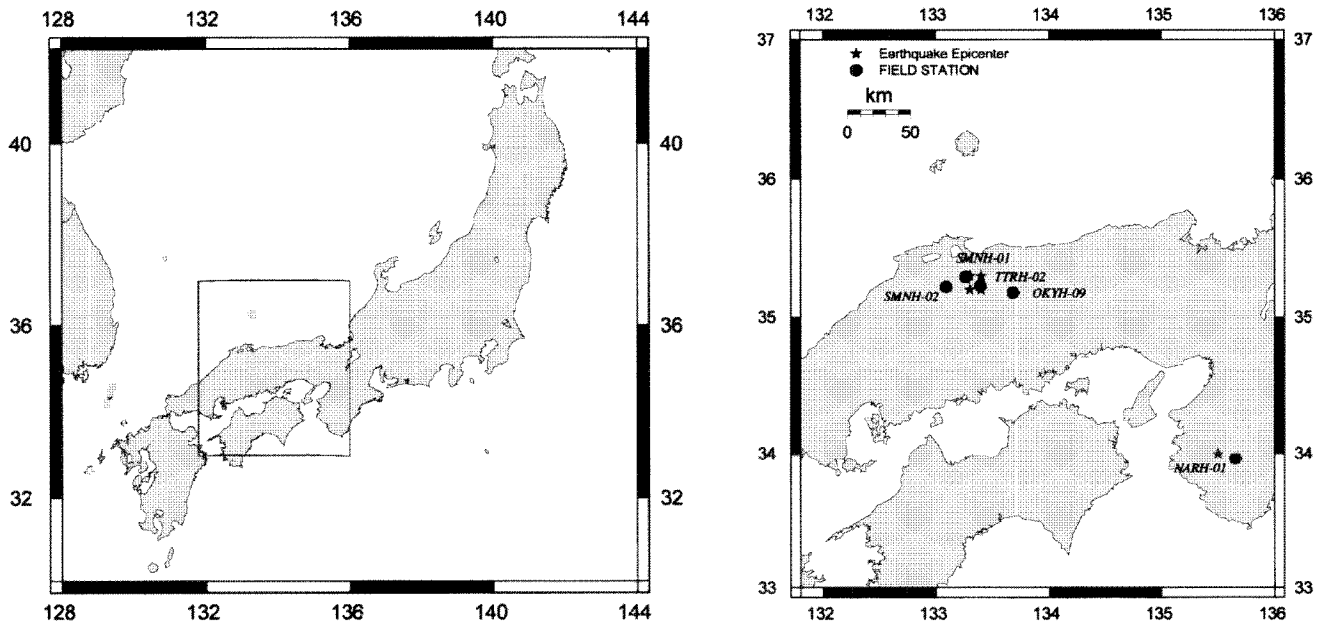


Figure 5. (Left) Map of Japan with the area (boxed) in which the selected events and boreholes are located. (Right) Close-up view of the boxed area.

nents of ground acceleration for this event recorded at TTRH02; this borehole recorded the strongest motions. All other events fall below the  $0.1g$   $P$ -wave acceleration level and are arranged in the order of decreasing  $P$ -wave acceleration. They are used for control purposes, as is the borehole NARH01.

The known common manifestation of nonlinearity in  $S$  waves is the shift in the resonance frequency to lower values and the reduction in amplification, as the amplitude of motions increases, characteristic of the hysteretic softening type of nonlinearity (Silva, 1986; Beresnev and Wen, 1996a; Field *et al.*, 1997; Dimitriu *et al.*, 2000). Figure 7 shows the  $S$ -wave nonlinearity clearly as a nonlinear response of the sand and gravel layer at TTRH02 borehole to the shear wave; the period of shear motion becomes visibly longer at horizontal components of the surface instrument compared to those in granite at depth. The significant decrease in the resonance frequency can be directly seen if the shear-wave uphole/downhole spectral ratio is compared to that in weak events (not reproduced here because manifestations of  $S$ -wave nonlinearity are rather well understood and beyond the scope of this article).

Patterns, similar to  $S$ -wave nonlinearity, can be seen in  $P$ -wave amplification for the Tottoriken-seibu event at boreholes OKYH09 (Fig. 6b), SMNH01 (Fig. 6c), and TTRH02 (Fig. 6h), or the boreholes that penetrated the soft soil material. A frequency shift of the main weak-motion amplification peak of up to  $0.7$  Hz (at OKYH09) is observed (cf. thick and thin lines); the reduction in amplification is also seen in Figure 6b and h. The magnitude of the frequency shift is comparable to that typically observed for shear waves (e.g., Beresnev *et al.*, 1998). The only borehole that does

not exhibit a visible shift for the same event is SMNH02 (Fig. 6g); however, this is the borehole drilled entirely in hard rock.

The amplifications measured at boreholes SMNH01 and TTRH02 for the intermediate events (overall peak acceleration exceeding  $0.1g$  but  $P$ -wave acceleration below  $0.1g$ ) are plotted in Figure 6d–f, i–l. The downward shift in the resonance frequency disappears for these events, supporting the argument that the shift observed for the strong event is caused by  $P$ -wave nonlinearity. Note that the increase in the strong-motion amplification (thick line) in Figure 6j at low frequencies is probably caused by some glitches in the data; however, visual inspection of the traces did not reveal any unusual features. Finally, Figure 6a provides one more control example. The thick line corresponds to another intermediate event, recorded by borehole NARH01, with peak  $P$ -wave acceleration of  $49$  cm/sec<sup>2</sup>. The borehole was drilled in soft slate material. The amplification function for this event virtually coincides with the average weak-motion amplification. We conclude that the shifts in the resonance frequency, seen in Figure 6 for the strongest (Tottoriken-seibu) event, are caused by the nonlinear soil response to compressional deformation. The nonlinearity in  $P$  waves is observable at the acceleration levels roughly exceeding  $0.1g$ . The manifestation of the effect is similar to that typically observed in  $S$  waves.

Beresnev and Wen (1995) came to a different conclusion when performing similar analyses for a strong event recorded by the Lotung borehole array in Taiwan drilled in soft sediments. There was no detectable difference between the location of the resonance peak nor the level of amplification between the weak and strong motions, calculated for



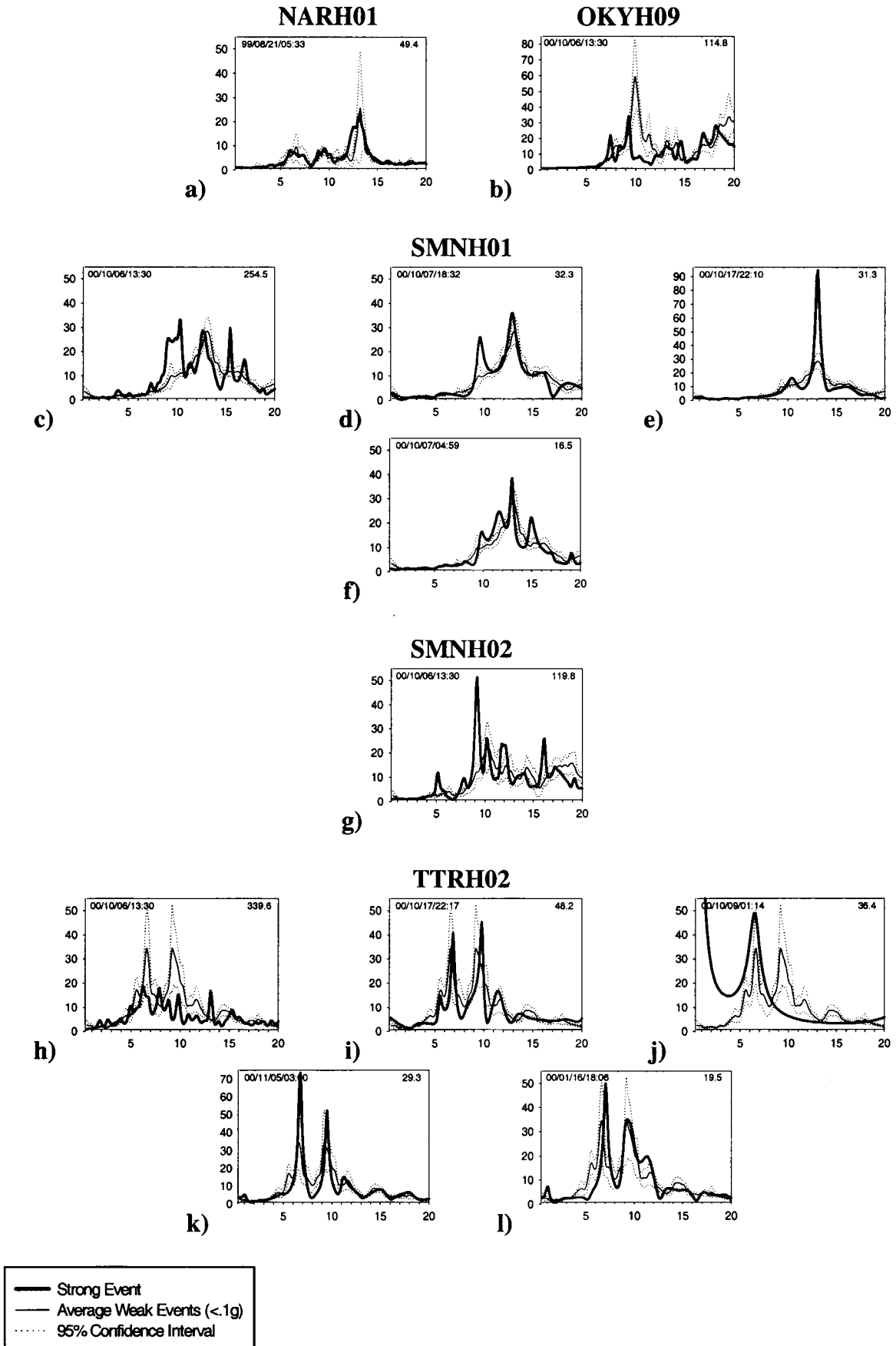




Figure 6. Empirical site amplification functions at KiK-net borehole sites. The horizontal axis is frequency in Hz. The boreholes are arranged in alphabetical order. The thin line shows the average weak-motion amplification for each borehole; the dotted line is the 95% confidence interval of the mean. The thick line is the amplification function for a strong event. The origin time of the strong event and its peak acceleration in *P*-wave window on the vertical component (in cm/sec<sup>2</sup>) are indicated in the upper left and right corners, respectively. For each borehole, the strong events are arranged in the order of decreasing *P*-wave acceleration; the weak-motion amplification function is the same.

the events selected using the same criterion. The peak *P*-wave acceleration was 109 cm/sec<sup>2</sup>, which is significantly lower than those observed in Figure 6c and h and slightly lower than that in Figure 6b. The KiK-net data provide evidence supporting the nonlinear response of soil to compressional deformation; to further constrain the characteristics of *P*-wave nonlinearity, similar analyses should be performed as more data are collected.

Reasonable caution should be exercised in ascertaining that the main weak-motion resonance peaks, observed as shifting in Figure 6b (OKYH09), 6c (SMNH01), and 6h (TTRH02), are associated with the transfer function of *P*, not *S*, waves, and consequently that we correctly attribute the shift phenomena to *P*-wave nonlinearity. To look into this issue, we calculated the theoretical spectral ratios between the surface and bottom instruments for the above boreholes of interest. The ratios were calculated using the reflection/transmission matrix method of Kennett and Kerry (1979), assuming a *P*-wave incident from below. The borehole *P*- and *S*-wave velocity profiles, used for the theoretical-

response calculations, are available from the KiK-net Web site and are reproduced in Figure 8. Densities ( $\rho$ ) were not reported; they were generated using the previously mentioned empirical Gardner's rule. Also, the absolute value of theoretical ratios will depend on the quality factors  $Q$  in the profile, which were not measured. However, the choice of  $Q$  is unimportant for the purposes of this analysis, since we are only interested in the frequency of the peaks and not their absolute value. We thus arbitrarily assumed  $Q$  to be 100 and 1000 in the soil and rock layers, respectively. The theoretical spectral ratios for the vertical component are presented in Figure 9 for two incidence angles, 0° and 10°.

Figure 9 shows that the main weak-motion resonance peaks observed in Figure 6 are the fundamental (lowest) resonances of the *P*-wave, with an almost exact match between the observed and theoretically calculated frequencies. The variation in the angle of incidence leaves the ratios nearly unaffected. This calculation supports the conclusion that we deal with the resonance in *P*-wave motions and that the shift is attributed to *P*-wave nonlinearity.

Using the observed resonance-frequency shifts ( $\Delta f$ ), the corresponding changes in the elastic moduli controlling *P*-wave velocity can be estimated. Using  $V_p = (M/\rho)^{1/2}$ , where  $M \equiv K + (4/3)\mu$ , and  $K$  and  $\mu$  are the bulk and shear moduli, respectively, the ratio between the strong-motion modulus ( $M_s$ ) and weak-motion modulus ( $M_w$ ) can be written as

$$M_s/M_w = (1 - \Delta f/f_w)^2, \quad (2)$$

where  $f_w$  is the weak-motion resonance frequency (Beresnev *et al.* [1998], their equation 2). The modulus  $M$  is the "constrained" modulus in geotechnical terminology. The surface compressional strain in *P*-wave window can be estimated from the observed peak vertical acceleration, predominant frequency, and near-surface *P*-wave velocity in the assump-

TTRH02 Event 00/10/06/13:30

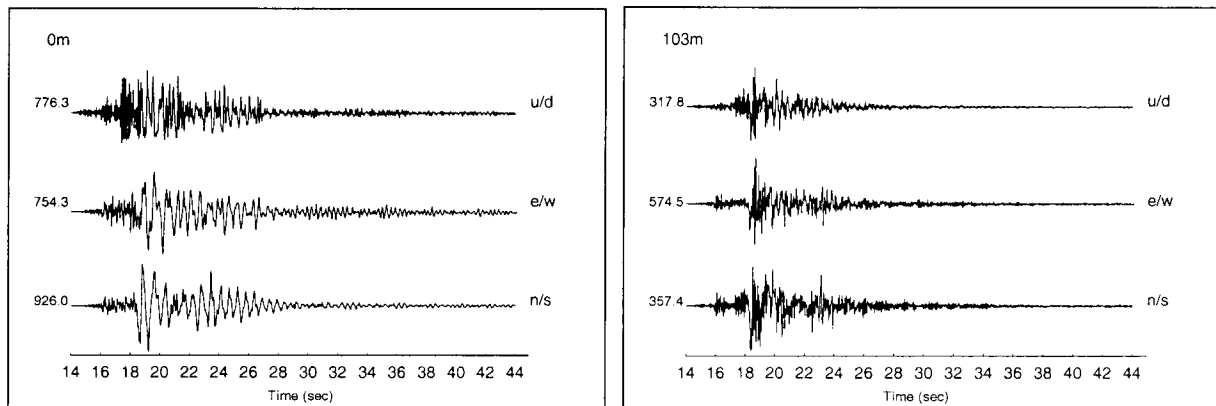


Figure 7. Three components of acceleration recorded by TTRH02 during the *M* 7.1 Tottori earthquake at the surface (*left*) and 103 m (*right*). The whole-trace maximum acceleration is listed to the left of the traces.

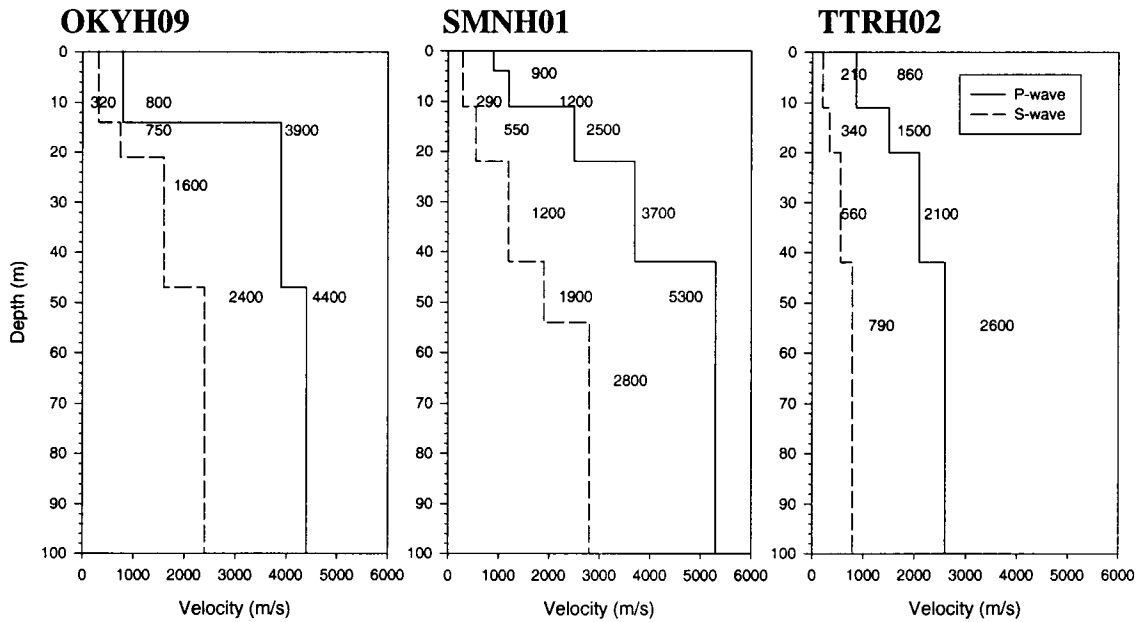


Figure 8. *P*- and *S*-wave velocity structures for the three KiK-net boreholes.

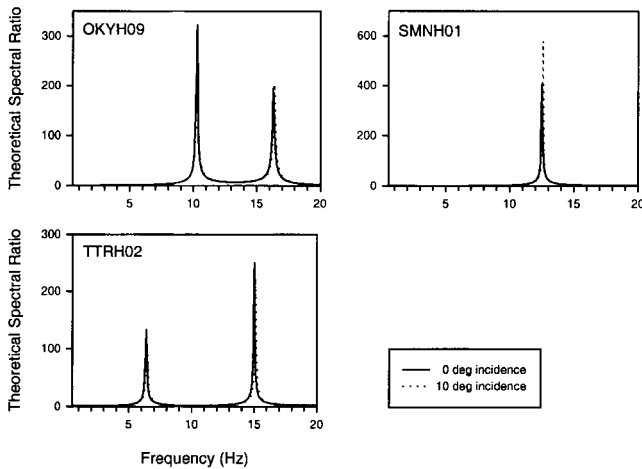


Figure 9. Theoretical *P*-wave spectral ratios between the surface and downhole instruments for the velocity profiles shown in Figure 8.

tion of a harmonic wave train, as discussed by Beresnev and Wen (1996b, their equation 15). We applied this approach to the frequency shifts observed in Figure 6b, c, and h. We also assumed that nonlinearity was nondetectable (modulus ratio of 1) in Figure 6a, d, and i, as the level of acceleration dropped. The results of these calculations are shown in Figure 10 (solid circles) as a chart of constrained-modulus ratio ( $M_s/M_w$ ) in the surficial layer as a function of strain amplitude at the surface. Table 2 summarizes the parameters used in computing the chart. The predominant frequency was calculated from the Fourier amplitude spectra, and the near-surface *P*-wave velocity was taken as the average over the top 10 m of the velocity profiles available from the KiK-net

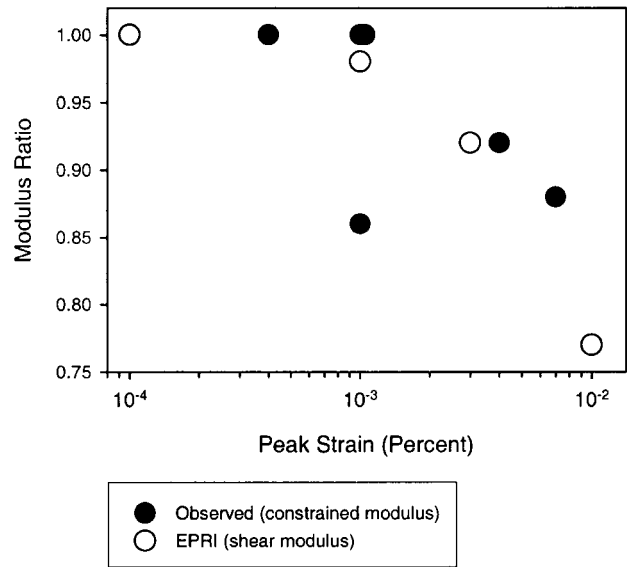


Figure 10. Constrained-modulus reduction effect (solid circles) from *P*-wave amplification data. The EPRI (1993) guidelines for shear-modulus reduction in sand are shown for reference (open circles).

Web site, to try to represent an average near-surface strain. The data in Figure 10 exhibit considerable scatter but illustrate the order of magnitude of the modulus-reduction effect. The compressional-strain level marking the transition between the linear and nonlinear responses ( $\sim 10^{-3}\%$ , Fig. 10) matches closely that for shear waves, as seen from the EPRI (1993) shear-modulus reduction guidelines for sand also reproduced in Figure 10 (open circles). The EPRI data shown are the average over the depth range of 0–15 m (0–

Table 2  
Parameters for Modulus-Reduction Curve Calculation

Borehole	$f_w$ (Hz)	$\Delta f$ (Hz)	$M_s/M_w$	Peak Vertical Acceleration (cm/sec <sup>2</sup> )	Predominant Frequency (Hz)	$P$ -wave Velocity (m/sec)	Compressional-Strain Amplitude (%)
NARH01	—	—	1	49.4	12.1	434	$1 \times 10^{-3}$
OKYH09	9.8	0.7	0.86	114.8	19.0	800	$1 \times 10^{-3}$
SMNH01	13.0	0.5	0.92	254.5	9.4	1050	$4 \times 10^{-3}$
SMNH01	—	—	1	32.4	10.7	1050	$4 \times 10^{-4}$
TTRH02	6.6	0.4	0.88	339.6	8.5	860	$7 \times 10^{-3}$
TTRH02	—	—	1	48.2	9.1	860	$1 \times 10^{-3}$

50 ft), to reflect the depth interval for which strains were computed. It is not clear whether the strain dependence of the constrained modulus is primarily caused by the respective change in the shear modulus ( $\mu$ ) or bulk modulus ( $K$ ), since the evaluation of  $M$  based on resonance frequency (controlled by  $P$ -wave velocity) does not allow separation of these contributions. However, it seems unlikely that compressional strain could significantly alter the shear modulus, so one could hypothesize that the reduction in  $M$  is primarily caused by the reduction in bulk modulus  $K$ , while  $\mu$  remains approximately constant. However, this is purely speculative at this time. The question of how much the bulk modulus  $K$  varies with strain remains open. Also, more data clearly are needed to better constrain the modulus reduction curve, such as in Figure 10, to the more specific shape similar to that developed for shear modulus. For example, there clearly exists one outlier (at the strain of  $10^{-3}\%$ ) that falls below the overall trend. The data shown should be considered preliminary and illustrating the order of magnitude of the effect.

It is clear that the degree of nonlinearity in compressional waves will depend significantly on the presence of fluids in porous space and will likely be limited to the sections above the water table. The  $P$ -wave velocity profiles shown in Figure 8 indicate that their top portions were above the water table (or at least were not fully saturated) at the time of measurements (velocities much lower than the speed of sound in water) and probably remained so during the Tottori earthquake, which may have made the detection of nonlinear response possible.

Nonlinearity in the propagation of  $P$  waves in earth materials is not something entirely new. The hysteretic softening nonlinearity has been reported for  $P$  waves with strain as low as  $10^{-8}$  propagating in dry sandstone (Guyer and Johnson, 1999). From those and the present findings, the compressional-wave nonlinearity seems to be of the same type known for shear waves. It has nevertheless not been observed before in strong ground motions with potential for engineering use.

## Conclusions

The results of this study suggest how the existing procedures for engineering development of site-specific vertical

motions could be modified. Contrary to the current view, we have found that shear ( $SV$ ) waves dominate vertical motions at frequencies up to approximately 10 Hz. For practical purposes, the design motions should thus be synthesized as near-vertically propagating  $SV$ , not  $P$ , waves, traversing the specified soil column. At frequencies below 10 Hz, which cover a broad range of engineering applications, the equivalent-linear analyses based on SHAKE could first be applied to synthesize the vertically propagating  $SH$  component. To convert the simulated  $SH$  motion into  $SV$  motion at a desired depth, and thus account for the inclined path of realistic  $SV$ -wave propagation, the empirical correction factors, such as developed by Darragh *et al.* (1999) (Fig. 3), could be used. The strain-dependent soil properties, serving as input to SHAKE, will be the same generally assumed for shear waves.

The simulation algorithm may become different if frequencies higher than  $\sim 10$  Hz are of interest. As Figures 1 and 2 show,  $P$  waves may become a significant contributor to the vertical motions at high frequencies. In this case, vertical motions could still be modeled with SHAKE, but as vertically propagating  $P$ -waves with strain-dependent soil properties specific for  $P$  waves. Corrections for nonvertical incidence, similar to the above V/H factors but specific for  $P$  waves, would have to be applied, which have not been developed yet.

Future studies should further investigate the  $P$ -wave strain-dependent soil properties (such as in Fig. 10), including damping, which should be developed independently of shear waves. There are indications that they may be similar to those for shear waves. It might also be true that even at higher frequencies, the vertical motions could still be modeled with sufficient accuracy as near-vertically propagating  $SV$  waves, which makes simulations at all frequencies straightforward to implement.

## Acknowledgments

This work was supported by the U.S. Geological Survey–National Earthquake Hazards Reduction Program (NEHRP) under Contract No. 01HQGR0027. The use of the data from the KiK-net network in Japan, available at <http://www.kik.bosai.go.jp>, is greatly appreciated. We are grateful to N. Gregor for stimulating discussions. The reflection/transmission FORTRAN code written by J.-C. Gariel was used. Figure 5 was prepared

with Generic Mapping Tools (GMT) (Wessel and Smith, 1998). We also thank two anonymous reviewers for their valuable comments on the article.

## References

- Aki, K., and P. Richards (1980). *Quantitative Seismology: Theory and Methods*, W. H. Freeman and Company, San Francisco, 932 pp.
- Beresnev, I. A., and K.-L. Wen (1995). *P*-wave amplification by near-surface deposits at different excitation levels, *Bull. Seism. Soc. Am.* **85**, 1490–1494.
- Beresnev, I. A., and K.-L. Wen (1996a). Nonlinear soil response—a reality? (a review), *Bull. Seism. Soc. Am.* **86**, 1964–1978.
- Beresnev, I. A., and K.-L. Wen (1996b). The possibility of observing nonlinear path effect in earthquake-induced seismic wave propagation, *Bull. Seism. Soc. Am.* **86**, 1028–1041.
- Beresnev, I. A., Field, E. H., Van Den Abeele, K., and Johnson, P. A. (1998). Magnitude of nonlinear sediment response in Los Angeles basin during the 1994 Northridge, California, earthquake, *Bull. Seism. Soc. Am.* **88**, 1079–1084.
- Bozorgnia, Y., M. Niazi, and K. W. Campbell (1995). Characteristics of free-field vertical ground motion during the Northridge earthquake, *Earthquake Spectra* **11**, 515–525.
- Darragh, B., W. Silva, and N. Gregor (1999). Bay Bridge downhole array analyses, report, submitted to Earth Mechanics, Inc., Fountain Valley, California.
- Dimitriu, P., N. Theodulidis, and P.-Y. Bard (2000). Evidence of nonlinear site response in HVSR from SMART1 (Taiwan) data, *Soil Dyn. Earthquake Eng.* **20**, 155–165.
- Electric Power Research Institute (EPRI) (1993). Guidelines for determining design basis ground motions: method and guidelines for estimating earthquake ground motion in Eastern North America, report EPRI TR-102293, Vol. 1, Palo Alto, California.
- Field, E. H., P. A. Johnson, I. A. Beresnev, and Y. Zeng (1997). Nonlinear ground-motion amplification by sediments during the 1994 Northridge earthquake, *Nature* **390**, 599–602.
- Guyot, R. A., and P. A. Johnson (1999). Nonlinear mesoscopic elasticity: evidence for a new class of materials, *Physics Today* **April**, 30–36.
- Idriss, I. M., and J. I. Sun (1992). User's manual for SHAKE91, a computer program for conducting equivalent linear seismic response analyses of horizontally layered soil deposits, Center for Geotechnical Modeling, Department of Civil and Environmental Engineering, University of California, Davis.
- Kennett, B. L. N., and N. J. Kerry (1979). Seismic waves in a stratified half space, *Geophys. J. R. Astr. Soc.* **57**, 557–583.
- Schnabel, P. B., J. Lysmer, and H. B. Seed (1972). SHAKE: A computer program for earthquake response analysis of horizontally layered sites, Rept. UCB/EERC 72/12, Earthquake Engineering Research Center, University of California, Berkeley.
- Sheriff, R. E., and L. P. Geldart (1995). *Exploration Seismology*, Second Ed., Cambridge University Press, New York, 592 pp.
- Silva, W. J. (1986). Soil response to earthquake ground motion, report prepared for Electric Power Research Institute, EPRI Research Project RP 2556-07.
- Silva, W. J. (1999). Characteristics of vertical strong ground motions for applications to engineering design, in *Proc. of the FHWA/NCEER Workshop on the National Rep. of Seismic Ground Motion for New and Existing Highway Facilities*, Technical Rept. NCEER-97-0010.
- Wessel, P., and W. H. F. Smith (1998). New, improved version of Generic Mapping Tools released, *EOS* **79**, 579.

Department of Geological and Atmospheric Sciences  
Iowa State University  
253 Science I  
Ames, Iowa 50011-3212  
[beresnev@iastate.edu](mailto:beresnev@iastate.edu)  
[amnigh@iastate.edu](mailto:amnigh@iastate.edu)  
(I.A.B., A.M.N.)

Pacific Engineering and Analysis  
311 Pomona Avenue  
E1 Cerrito, California 94530  
[pacificengineering@juno.com](mailto:pacificengineering@juno.com)  
(W.J.S.)

Manuscript received 11 January 2002.